ELSEVIER

'Brittle' shear zones in experimentally deformed quartz single crystals

Martine G.C. Vernooij *, Karsten Kunze, Bas den Brok

ETH Zürich Geologisches Institut, Leonhardstrasse 19 (LEB), CH-8092 Zürich, Switzerland

Abstract

Intracrystalline shear zones developed in a quartz single crystal that was experimentally deformed to 26% finite strain under conditions favourable for macroscopically ductile deformation. The crystal was uniaxially compressed parallel to $\langle c \rangle$, in the presence of 1 vol.% of added water, at a temperature of 800 °C, a confining pressure of 1200 MPa and a strain rate of $10^{-6}\,\mathrm{s}^{-1}$. We investigated how the shear zones initiated and how their structure evolved with ongoing deformation. Detailed crystallographic orientation analyses were carried out with the help of the electron backscatter diffraction (EBSD) technique and complemented by transmission electron microscopy (TEM). The shear zones appeared to develop along planar microcracks oriented parallel to crystallographic rhomb planes. Further microcracking resulted in cataclastic shear zone development. New grains developed by rotation of fracture fragments. The rotation of the fragments in the shear direction was probably facilitated by the high water pressure and the relatively high porosity in the shear zone. Shear zones finally exhibit a strong crystallographic preferred orientation (CPO). Our results suggest that cataclastic deformation processes may lead to shear zone development. The CPO developed within the shear zones through dynamic recrystallisation, i.e. new grains with $\langle c \rangle$ oriented approximately perpendicular to the shear zone boundary grew at the cost of other new grains.

1. Introduction

Deformation in the Earth's crust is generally inhomogeneous and often localised in shear zones (Ramsay, 1980). Shear zones are very common in quartz-rich rocks deformed in the middle and lower crust. Their geometry, microstructures and crystallographic preferred orientations (CPOs) often possess clear asymmetries with respect to the macroscopic foliation and lineation. Therefore they preserve information about the deformation history and the relative sense of movement.

Still little is known about how shear zones initiate and evolve once they have formed. It has been argued that shear zones can nucleate on grain scale brittle fractures (Segall and Simpson, 1986; Ralser, 1990; van Daalen et al., 1999). It is not yet clear when in the deformation history such fractures are introduced: during a preceding phase of extension (van Daalen

et al., 1999), during a preceding phase of compression (Segall and Simpson, 1986; Ralser, 1990), or simultaneously by progressive deformation and shear zone development. The subsequent deformation accommodated by the shear zones has mostly been assumed to be crystal-plastic, because the (small) new grains within the shear zones exhibit a microstructure commonly interpreted to have formed by dynamic recrystallisation. Models that aimed at understanding dynamic recrystallisation are mainly based on two processes: (1) subgrain rotation, and (2) grain boundary migration (Urai et al., 1986). However, local analyses of new 'recrystallised' grains in naturally deformed dolomite and calcite shear zones have shown that the misorientation relationships between parent and recrystallised grains cannot easily be explained by simple models of subgrain rotation and grain boundary migration recrystallisation alone (Leiss and Barber, 1999; Bestmann and Prior, 2003). Thus, other processes were discussed to be invoked: (1) rigid body rotation, (2) nucleation, and (3) diffusion accommodated grain boundary sliding. These processes may exert an important control on the formation of new grains.

This study focuses on how microscopic shear zones nucleate in quartz deformed in the presence of water and on the role of dynamic recrystallisation during the progressive deformation

* Present address: EMPA, Swiss Federal Laboratory for Materials Science and Technology, Überlandstrasse 129, CH–8600 Dübendorf, Switzerland. Tel.: +41 (0)44 823 4379; fax: +41 (0)44 821 6244.

E-mail address: vernooij@alumni.ethz.ch (M.G.C. Vernooij).

in these zones. We studied conjugate intracrystalline shear zones that developed during experimental deformation at high pressure (1.2 GPa) and temperature (800 °C) in a natural quartz single crystal with the compression direction (σ_1) parallel to $\langle c \rangle$. Various crystallographically aligned shear zones reflecting different stages in the shear zone evolution are observed in one single sample that was deformed at an approximately constant strain rate of 10^{-6} s^{-1}; so called (1) initial shear zones, (2) transitional shear zones, and (3) mature shear zones. Initial shear zones consist of single chains of (sub)grains, transitional shear zones consist of several rows of new grains that have a common rotation axis and mature shear zones consist of several rows of new grains with no common rotation axis, but with a strong c-axis maximum at 45° to σ_1. The shear zones were analysed using detailed orientation and misorientation analysis based on electron backscatter diffraction (EBSD) data that are presented in orientation maps, misorientation profiles and pole figures. The EBSD observations were verified by transmission electron microscope (TEM) images.

2. Methods

2.1. Sample description

In the course of a larger study (Vernooij, 2005; Vernooij and Langenhorst, 2005), quartz single crystal samples were deformed in different starting orientations (σ_1//$\langle c \rangle$, σ_1//$\langle o+ \rangle$, σ_1//$\langle a \rangle$ and $\sigma_1 \sim \perp \{r\}$) with and without added water. Intracrystalline shear zones developed only in the sample that was deformed parallel to $\langle c \rangle$ and only in the presence of water. This particular sample (GRZ25) is further described in this paper. The sample was cored from a natural quartz single crystal from Arizona, using a diamond coring tool with water as a lubricant. The crystal was transparent, clear of fluid inclusions and without optically visible defects. The internal water content of the crystal was ~ 0.002 wt% (determined by Fourier transform infrared (FTIR) spectroscopy and calculated using the calibration of Paterson (1982)). The ends of the sample (measuring 5.85 mm in diameter and 12.1 mm in length) were ground flat and parallel. The sample was weld-sealed in a gold capsule together with 1 vol.% of distilled water following the procedure described by den Brok (1992).

2.2. Deformation test

The deformation experiment was performed in a Tullis-modified solid medium Griggs deformation apparatus (Vernooij and Langenhorst, 2005). The sample assembly was brought to a confining pressure of 1.2 GPa and a temperature of 800 °C within 7.5 h following the water isochore of 1 g cm^{-3} as closely as possible. After an equilibration period of 17 h it was loaded (no 'cold hit') and deformed in uniaxial compression at a constant axial displacement rate corresponding to an initial strain rate of 1.1×10^{-6} s^{-1}. It must be noted here that this is an average value and that locally different strain rates are expected in some parts of the sample as indicated by the clearly inhomogeneous microstructure. After deformation of the sample, pressure and

temperature were lowered in 1 h, again closely following the 1 g cm^{-3} water isochore. The measured axial displacement was corrected for apparatus distortion (20 μm kN^{-1} at 800 °C and 1.2 GPa). The axial load was not corrected for friction increase during the experiment. Differential stress was calculated using the initial cross-section of the sample. A finite strain of 26% was determined based on the final sample length measured ex-situ at room temperature and pressure.

2.3. Sample preparation for analysis

During deformation, the cylindrical sample developed a slightly elliptical cross-section. To prepare the sections for microscopical analysis, the sample was cut parallel to the long axis of the ellipse and parallel to the compression direction. One half of the sample was impregnated with Epofix so that a thin section could be polished (using 0.05 μm alumina suspension) without loosing much material. The other half of the sample was used to prepare a 200-μm-thick section for EBSD analysis and to prepare another thin section for TEM analysis. The thick section was mechanically polished like both thin sections and subsequently lapped for 8 h using an alkaline colloidal silica suspension (particle size 25 nm). To avoid charging, the EBSD thick section was coated with a ~ 4 nm carbon layer and covered around the lapped sample surface with silver paint. The areas that were selected for TEM analysis on the non-impregnated thin section were thinned by ion-milling until electron transparency was reached (~ 0.1–0.2 μm thickness). The TEM sample was also carbon coated to avoid charging problems. The TEM analyses were performed with a Philips CM20 FEG TEM, operating at 200 kV, at the Bayerisches Geoinstitut at the University of Bayreuth, Germany. Conventional bright-field and dark-field imaging techniques were used to observe and characterise the microstructures.

2.4. EBSD data acquisition and analysis

Full crystallographic orientation data were obtained from automatically indexed electron backscatter diffraction (EBSD) patterns (Adams et al., 1993; Prior et al., 1999). EBSD patterns were acquired using an EDAX–TSL DigiviewFW camera system attached to an SEM CamScan CS44LB. The EBSD patterns were obtained using 15 kV acceleration voltage, 35 mm working distance, ~ 3 nA beam current and 70° sample tilt. EBSD scans were run on square grids with a step size of 0.5 μm at a typical scan speed of nine patterns per second. The patterns were collected and indexed with the commercial TSL software OIM DC 3.5™ and analysed with OIM Analysis 3.0™ and 3.5™.

Recorded data contain the crystal orientation of trigonal quartz (given by three Euler angles), the xy-coordinates of the spot on the sample and an indexing reliability parameter (confidence index (CI) between 0 and 1). The analyses show a large number of data with a high reliability (CI > 0.1). The obtained data are presented in orientation maps, a pattern

quality map, misorientation profiles, misorientation distributions and pole figures.

In orientation maps, the colour of each pixel corresponds to the crystal direction parallel to the compression axis (σ_1) in the corresponding colour key. In pattern quality maps, grey shades relate to band sharpness of the EBSD-pattern. Since these pattern quality maps reproduce surface damage, fractures and (sub)grain boundaries, they form an additional image of the microstructure and are useful to verify the reliability of the orientation maps.

The deformation experiment was performed close to the transition temperature from α- to β-quartz, which is 850 °C at 1200 MPa (Bagdassarov and Delépine, 2004). Therefore it is not clear whether the Dauphiné twins that are repeatedly indexed are induced during deformation or during cooling (the starting material was free of Dauphiné twins). Potentially ambiguous results from misindexing in Dauphiné twin orientations are avoided by treating the quartz data with hexagonal crystal symmetry in all post-processing steps.

The raw orientation maps for hexagonal quartz still contain a number of erroneous data, especially along (sub)grain boundaries, on surface scratches, holes or other surface artefacts where the pattern quality was low. The OIM software provides a simple algorithm to clean these erroneous data by replacing them by the most common neighbouring orientation. Because the step-size is much smaller than the grain size, most erroneous data can be identified as single pixels that are different from all surrounding points. The cleaned data are further used in all the analyses.

Misorientation profiles were drawn along lines in the cleaned orientation maps. The misorientation angle between adjacent points along these lines was calculated by selecting the minimum angle that enables the lattice of one point to be rotated into that of the other (Wheeler et al., 2001). The data along the lines were selected, plotted in equal area, upper hemisphere pole figures and used to specify rotation paths and rotation axes. We developed a program to calculate the best-fit rotation axes based on the determination of second order moments of the orientation distributions, following derivations by Prentice (1986) and Kunze and Schaeben (2004).

The misorientation between nearest neighbour grid points was also determined as the rotation with the smallest possible rotation angle in the unit triangle. The rotation axes of the misorientations are plotted with respect to the crystal and to the sample reference frame, respectively, for fixed intervals of rotation angle.

3. Results

3.1. Mechanical data

The stress–strain curve (Fig. 1) shows an initial stage of linear work hardening until a peak stress of ~410 MPa was reached at ~2% bulk strain. After that there is a stage of weakening until ~10% bulk strain, followed by a stage of non-linear work hardening until a constant flow stress was reached (~470 MPa) beyond ~22% bulk strain.

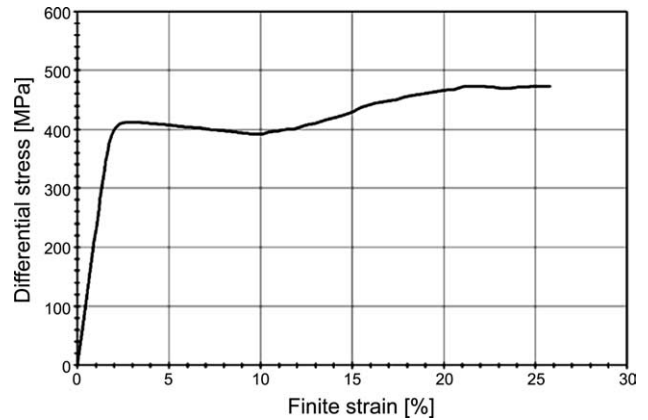Fig. 1. Differential stress versus strain curve for the deformation experiment (GRZ25). The sample was deformed with $\sigma_1//\langle c \rangle$, at 800 °C, a confining pressure of 1.2 GPa and an approximately constant strain rate of 1.1×10^{-6} s^{-1}.

3.2. Microstructures

The sample strain is particularly concentrated at the lower end of the sample (Fig. 2) in a wedge shaped sector containing a dense network of conjugate intracrystalline shear zones. These shear zones are typically up to 10 μm wide and cross-cut the sample in diagonal directions (Fig. 3a). In general, shear zones dipping to the right record a dextral offset (Fig. 2) and
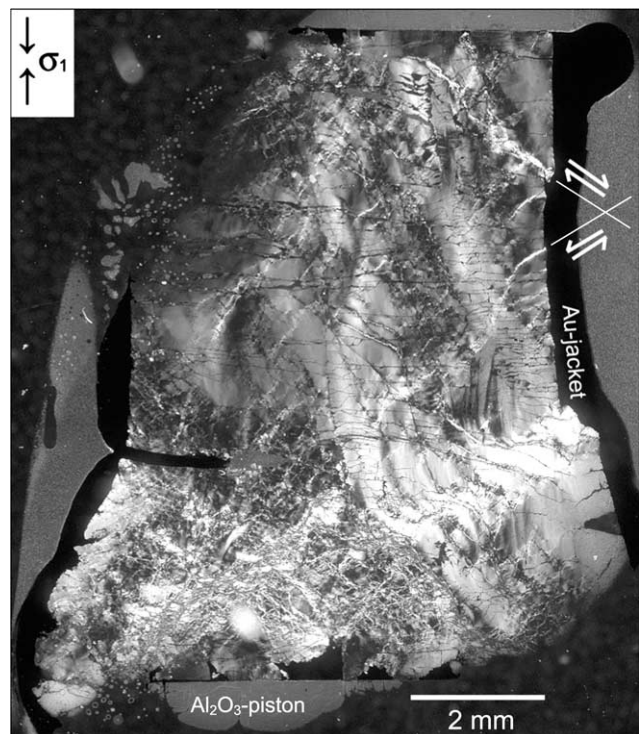

Fig. 2. Micrograph of heterogeneously deformed sample (GRZ25) in cross polarised light. Most strain is accommodated at the lower end of the sample along a wedge shaped network of conjugate sets of shear zones. Some shear zones at the sample edge reveal the sense of shear (white arrows). In the less deformed part of the sample, zones of undulatory extinction developed approximately parallel to $\langle c \rangle$.
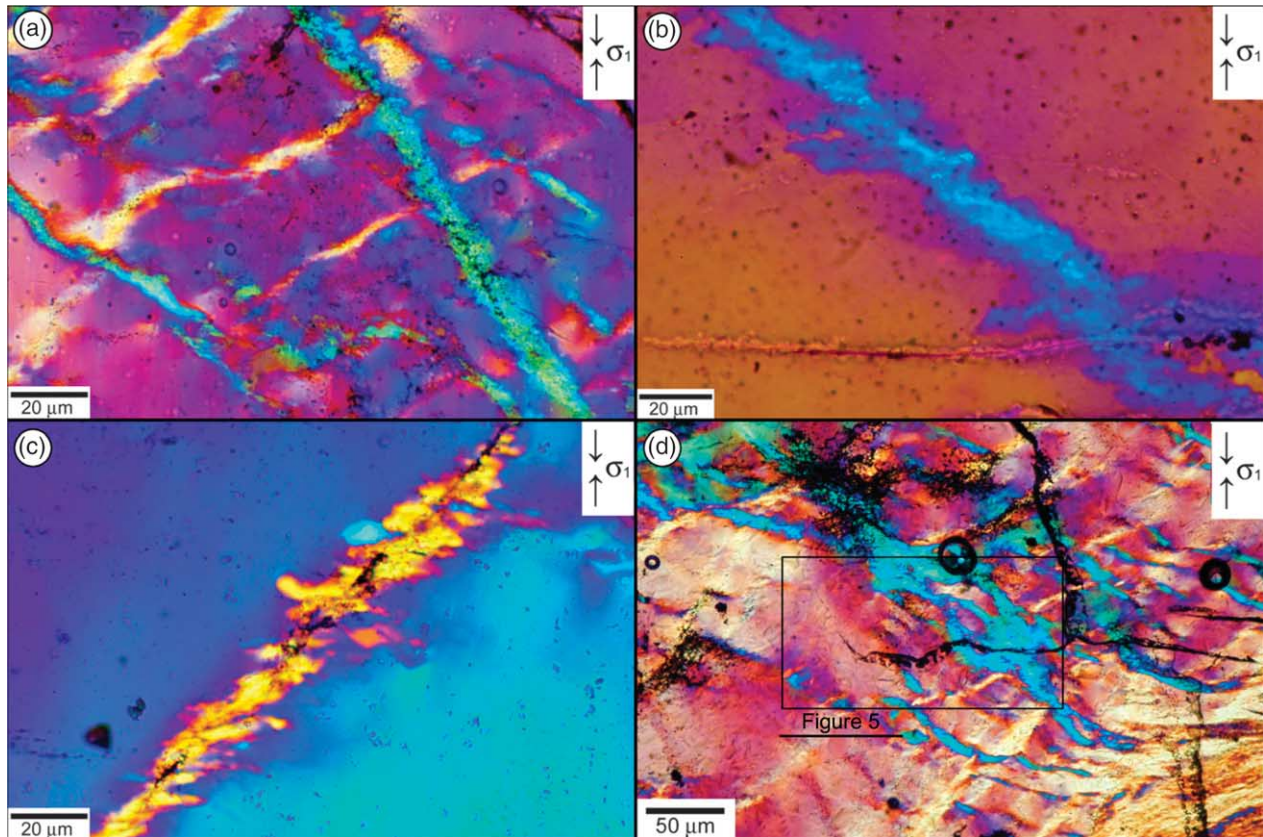
Fig. 3. Light micrographs (crossed polarisers; gypsum plate) of experimentally produced intracrystalline shear zones in sample (GRZ25) deformed parallel to $\langle c \rangle$ at 800 °C, confining pressure of 1.2 GPa and approximately constant strain rate of $1.1 \times 10^{-6} \, \text{s}^{-1}$. The tiny new grains in the shear zones have a distinctly different crystallographic orientation than the surrounding host material. Shear zones are traced by fluid inclusions. Grains near the shear zone boundaries are elongate perpendicular to σ_1. (a) Conjugate sets of shear zones from the high strain end of the sample. (b) Shear zones dipping to the right are dextral and have a blue interference colour. (c) Shear zones dipping to the left are sinistral and have a yellow interference colour. (d) Part of the sample with shear zones that reflect different stages of shear zone development. Box indicates the location of the EBSD scan of Fig. 5.

have a blue colour (Fig. 3b) under crossed polarisers with the gypsum plate; shear zones dipping to the left have sinistral displacement (Fig. 2) and a yellow colour (Fig. 3c). Grains in the middle of the shear zones are too tiny to be optically distinguishable. Grains near the shear zone boundaries and within the matrix are optically strain-free (no undulatory extinction) and have a sub-euhedral shape (Fig. 3b and c). They are slightly elongated with their long axis perpendicular to the shortening direction, i.e. at 40–45° to the shear zone boundary. The shear zones are traced by trails of very tiny fluid inclusions (Fig. 3a and c) and encompass blocks of the host crystal with low strain deformation microstructures, i.e. continuous undulatory extinction and deformation lamellae. One area with conjugate sets of shear zones that reflect different stages of shear zone evolution was chosen for detailed EBSD analysis (Fig. 3d).

TEM images reveal that the interiors of the shear zones consist of $\sim 3 \, \mu\text{m}$ diameter new grains (Fig. 4a). These grains have a variety of crystallographic orientations, straight grain boundaries and round edges. The grain boundaries are decorated with $< \sim 0.1 \, \mu\text{m}$ voids. Numerous larger voids (up to $\sim 1 \, \mu\text{m}$) occupy triple junctions between the new grains (Fig. 4a and b) indicating a high (presumably fluid-filled) porosity within the shear zones. Within the new grains there is

a high dislocation density, especially at the grain contacts (Fig. 4b). The dislocations are curved, tangled and sometimes occupy straight subgrain walls.

Curved and tangled dislocations are also observed within the host domains of the sample. The dislocation density within the host is high ($10^{10} \, \text{cm}^{-2}$). TEM images were taken with diffraction vectors $\mathbf{g} = 10\bar{1}1$, $\mathbf{g} = 10\bar{1}0$ and $\mathbf{g} = 0003$ in order to determine the Burgers vectors by applying the $\mathbf{g} \cdot \mathbf{b} = 0$ criterion. Most dislocations are out of contrast with $\mathbf{g} = 10\bar{1}0$ and $\mathbf{g} = 0003$ but are well visible with $\mathbf{g} = 10\bar{1}1$ (Fig. 4c). Therefore the Burgers vector of the free dislocations is mostly $\mathbf{b} = 1/3\langle 11\bar{2}0 \rangle$. Within the host domains, several straight walls that are decorated with very tiny voids ($\sim 0.1 \, \mu\text{m}$) occur (Fig. 4c). They are oriented parallel to the shear zones and separate areas of slightly different dislocation density.

3.3. Crystallographic orientations

3.3.1. Orientation maps

The orientation maps and pattern quality map (Fig. 5) reproduce the optical micrograph (Fig. 3d) accurately. Several different microstructures can be distinguished: (1) gradual orientation changes within the host crystal, (2) aligned small angle boundaries within the host crystal, (3) initial shear zones
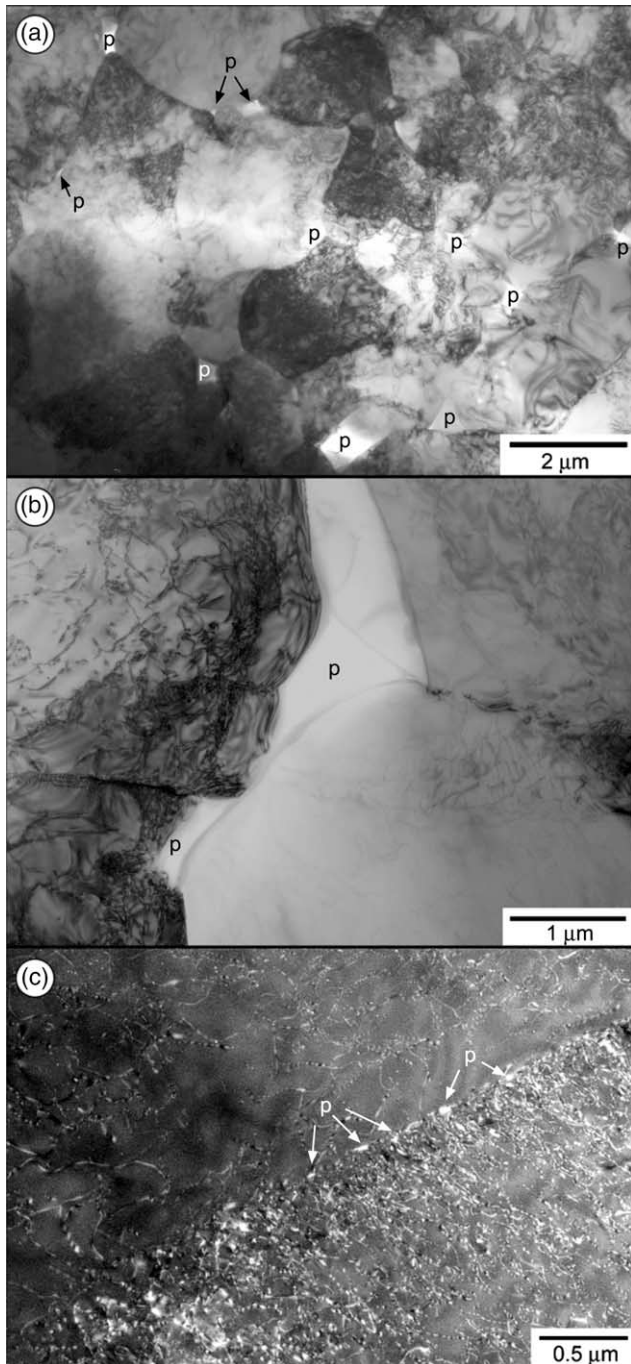
Fig. 4. TEM micrographs from the shear zones. (a) Bright field TEM micrograph of new grains and voids (marked with 'p') within the interior of a shear zone in sample GRZ25. The new grains have straight as well as curved grain boundaries; relatively large numbers of pores are present. (b) Bright field TEM micrograph of triple junction between three new grains. A relatively high density of tangled dislocations and subgrain walls occurs close to the grain boundaries. (c) Dark field TEM micrograph ($\mathbf{g} = 10\bar{1}1$) of straight wall within the host domain. Tangled and curved dislocations are distributed through the host domains. Walls that are decorated with tiny voids cross-cut the host domains. These walls are approximately parallel to the shear zones.

consisting of single chains of new (sub)grains along oriented subgrain walls, (4) conjugate sets of transitional and mature shear zones with several rows of new grains, and (5) isolated pockets of new grains.

The orientation map (Fig. 5a) marks nearest neighbour misorientation angles for different angular intervals, thus indicating and classifying the boundaries. These boundaries are also visible in the pattern quality map (Fig. 5b) because the data points on subgrain and grain boundaries have a lower pattern quality than those in the grain interior. Away from the shear zones, the orientation of the host crystal changes with small spatial gradients, i.e. misorientations below 2° between nearest neighbours. Approaching the shear zones, subgrain boundaries with misorientations of 2° to 10° are observed, which are either aligned more or less parallel or at $\sim$45° to the σ_1-direction. Within the shear zones, tiny new grains (average size 2.5 μm) are distinguished by high angle grain boundaries, as classified according to White (1977) for misorientation angles $>$10°. The transition in orientation between the new grains within the shear zones and the host crystal is sudden (misorientation almost exclusively $>$15°). Subgrains in the host crystal are generally larger than the new grains within the shear zones.

Another derived map (Fig. 5c) displays the angle of the *c*-axes in the deformed sample with respect to the starting orientation of the sample ($\langle c \rangle // \sigma_1$). It illustrates that (1) the angle of rotation increases towards the middle of the shear zone, (2) the angle of rotation is not constant along the shear zones, and (3) the largest angles (up to 90°) are observed within the largest shear zones.

3.3.2. Zone A: initial shear zones

The orientation map of zone A (Fig. 6a) shows two host blocks that are separated by three parallel distorted zones. Each of these zones contains a single array of aligned subgrains and a few new grains that are equal in size but much smaller than the host blocks. The zones are approximately parallel to the trace of one of the rhomb planes in the surrounding host domain. The new grains have homogeneous intracrystalline orientations, thus are nominally strain-free. The subgrains display gradual internal orientation changes, similar to gradual rotations within the host blocks. The host crystal orientation shows gradual clockwise and anticlockwise dispersion of up to 20° around an axis perpendicular to σ_1 (Fig. 7a). The orientations of the few new grains scatter widely around the host orientation (Fig. 7a). The misorientation profile (Fig. 8) illustrates gradual reorientation of the host crystal with point to point misorientations less than 2°. The pole figures (Fig. 8) illustrate that this reorientation corresponds to an anticlockwise rotation around a flat lying axis that is near $\langle a \rangle$ and $\{m\}$, but deviates from common low-index crystal directions. The misorientation axis and the sense of rotation changed where a high angle boundary (20°) is crossed (i.e. at the transition from host crystal into a new grain within the shear zone).

3.3.3. Zone B: dextral mature shear zones

The orientation map of zone B (Fig. 6b) shows two mature dextral shear zones that embody several arrays of new grains with fairly constant sizes. The shear zones are
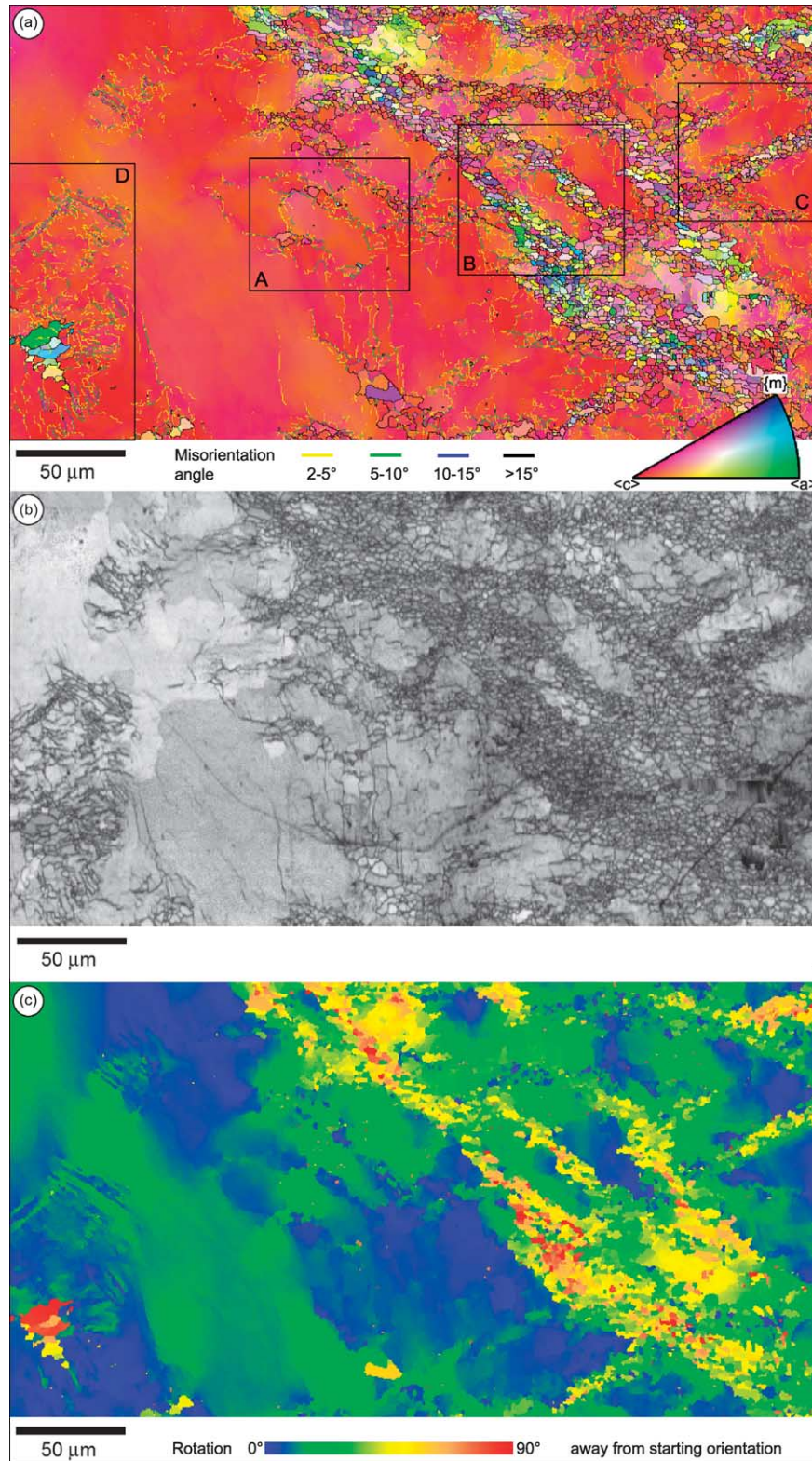
Fig. 5. Orientation maps from EBSD scans. The raw data were processed by substitution of likely misindexed data. (a) Orientation map colour coded corresponding to the inverse pole figure colour key (inset); colour represents the crystal direction that is parallel to σ_1. To highlight (sub)grain boundaries, nearest neighbour misorientations are colour coded according to four intervals of misorientation angle. Shear zones consist of tiny grains with high angle grain boundaries ($>10°$). The host crystal shows gradual rotations and aligned subgrain boundaries. Boxes indicate the locations of the areas that are analysed in detail and are shown in Fig. 6. (b) Pattern quality map. Grey shades relate to band sharpness of the EBSD pattern. The pattern quality map reproduces surface damage, fractures and (sub)grain boundaries. (c) Orientation map, colour shaded according to the angle between $\langle c \rangle$ and the starting orientation of the sample ($\sigma_1 // \langle c \rangle$). The isolated new grains and the new grains in the centres of the shear zones have c-axes that are up to $90°$ away from the starting orientation.
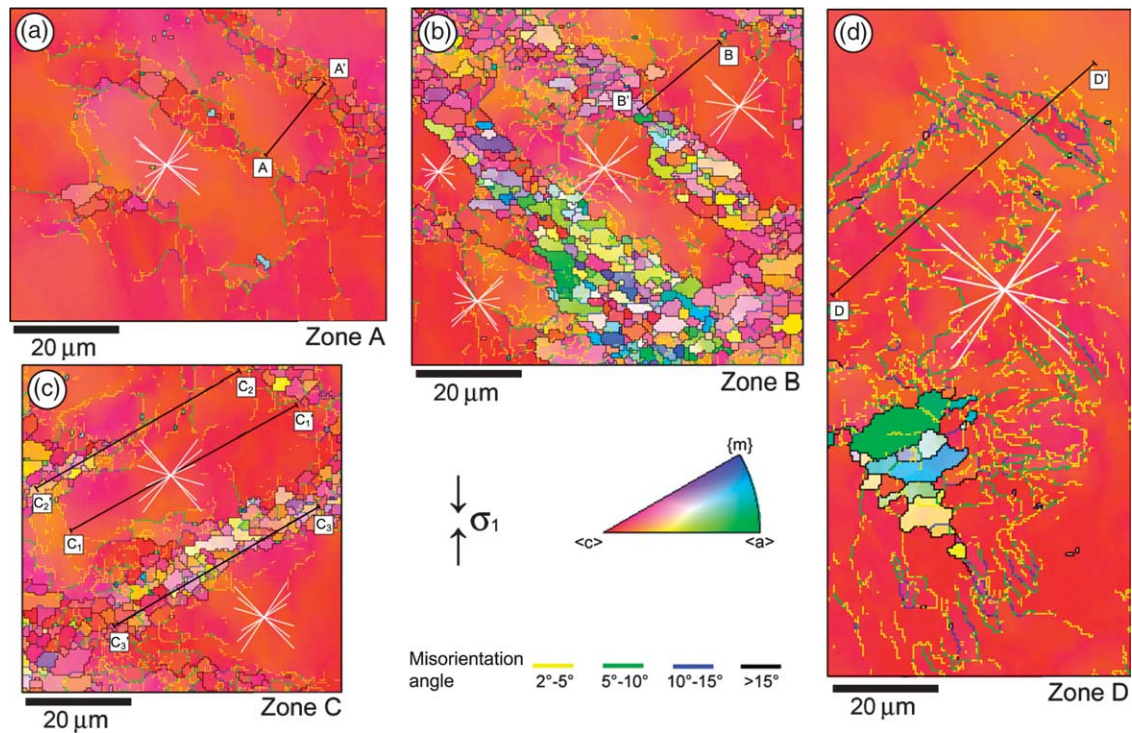
Fig. 6. Processed orientation maps of areas that are analysed in detail. Maps are colour coded corresponding to the inverse pole figure colour key. Grain boundary misorientations are colour coded according to misorientation angle between nearest neighbours. Straight black lines indicate the positions of misorientation profiles. White lines correspond to traces of rhomb planes (intersection line with sample surface). (a) Zone A, initial shear zone, (b) zone B, mature dextral shear zone, (c) zone C, mature sinistral shear zone and transitional shear zone, and (d) zone D, isolated pocket with new grains.

again parallel to the traces of rhomb planes in the flanking host domains. The grains within the shear zones are elongated perpendicular to σ_1 at $\sim 45°$ to the shear zone boundary with aspect ratio about 2:1. Near the shear zone boundary, new grains seem to have grown into the host domains. The host blocks next to the two shear zones are highly deformed and contain several 2–10° subgrain boundaries, which separate subgrains with different sizes that are generally larger than the new grains within the shear zones. New grains are strain-free; subgrains and host crystal show gradual lattice bending. The host lattice spreads roughly 20° away from the starting orientation in all directions (Fig. 7b). The new grains show an enormous spread of up to 90° away from the host orientation, with *c*-axes almost exclusively displaced in a clockwise sense. The crystallographic orientations of the new grains in the wider shear zone (lower left) are scattered further away from the host orientation than the crystallographic orientations of the new grains in the more narrow shear zone (upper right). The misorientation profile (Fig. 9) illustrates the counterclockwise rotation of the host lattice around an axis close to the pole to {*m*} lying perpendicular to σ_1. Before entering the shear zone, the profile crosses a subgrain boundary, which still has the same misorientation axis as the host lattice. The crystallographic rotation path of the new grain, however, is inconsistent with that of the host lattice and the subgrain.

3.3.4. Zone C: sinistral mature shear zone and sinistral transitional shear zone

In the orientation map of zone C (Fig. 6c), a sinistral mature shear zone (centre right) is displayed with a transitional shear zone (upper left) parallel to it. This transitional shear zone is an initial micro shear zone in the upper right, which develops into a mature zone towards the left. The mature shear zone consists of several arrays of new grains with elongated shapes and high angle grain boundaries as in zone B (Fig. 6b). Both shear zones are parallel to traces of rhomb planes within the adjacent host lattice. The host lattice shows gradual orientation changes and several subgrain boundaries near the contact with the shear zones. The orientation of the host lattice spreads away from the starting orientation into various directions with a maximum rotation of $\sim 20°$ (Fig. 7c). In the sinistral mature shear zone, the new grains show a large spread up to about 60° away from the host orientation, with *c*-axes almost exclusively displaced in an anticlockwise manner. Misorientation profiles show that the reorientation in the host lattice (Fig. 10a) is gradual with maximum point to point misorientations less than 2° and a counterclockwise rotation around an axis that is close to the pole to {*m*}. In the profile parallel to the transitional shear zone (Fig. 10b), the new grains gradually rotate away from the starting orientation (maximum point to point misorientation of 15°) instead of the larger jumps in crystallographic orientation that were observed in the misorientation profiles perpendicular to the shear zones (Figs. 8 and 9). The orientations of the new grains scatter considerably in all directions, but the calculated
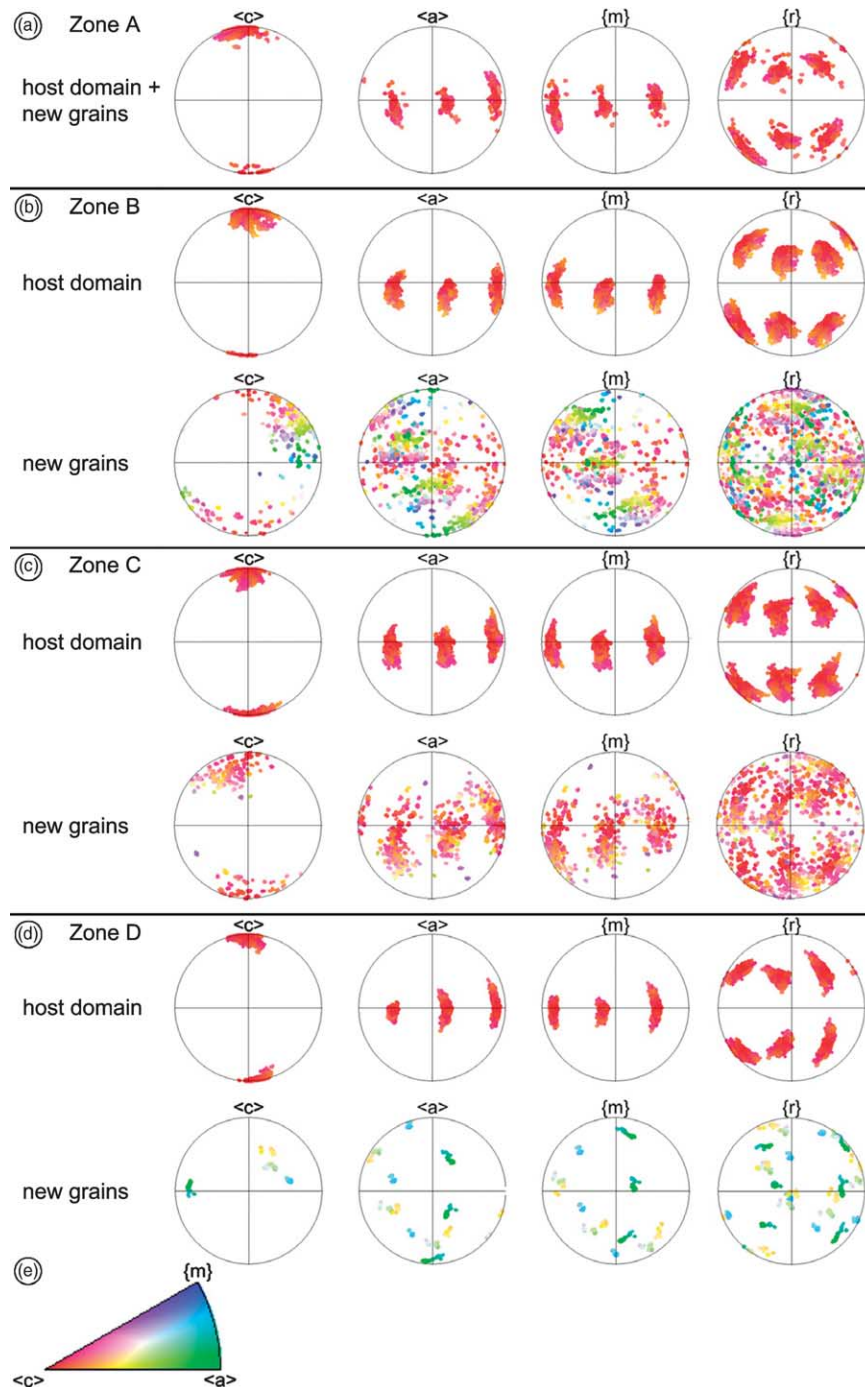
Fig. 7. Pole figures (equal area, upper hemisphere) of the host domains and domains with new grains (defined by grain boundary misorientation >10° to the host). Figures are coloured according to the colour key (e), which is the same as in Figs. 5 and 6. (a) Zone A, initial shear zone, (b) zone B, mature dextral shear zone, (c) zone C, mature sinistral shear zone and transitional shear zone, and (d) zone D, isolated pocket with new grains.

mean rotation axis of the new grains is close to the pole to {m} as well, which is, however, one of the other {m}-poles than the one in the adjacent host lattice. Both the rotation axes of the host crystal and of the new grains in the transitional shear zone are perpendicular to σ_1. The misorientation profile through the mature shear zone (Fig. 10c) shows large angle jumps between grains and hardly any orientation spread within the new grains, regardless of whether this profile was taken parallel or perpendicular to the shear zone. No common rotation axis of

the grains in the mature shear zone could be reliably inferred because of the large spread of the data, which cluster around an anticlockwise rotated orientation.

3.3.5. Zone D: isolated pockets of new grains

The orientation map of zone D shows a patch of isolated new grains in a deformed host lattice (Fig. 6d). Subgrain boundaries with angles of 5–15° are aligned parallel to the intersection lines of rhomb planes in the host crystal. The isolated new grains (average size of ∼10 μm) are larger than
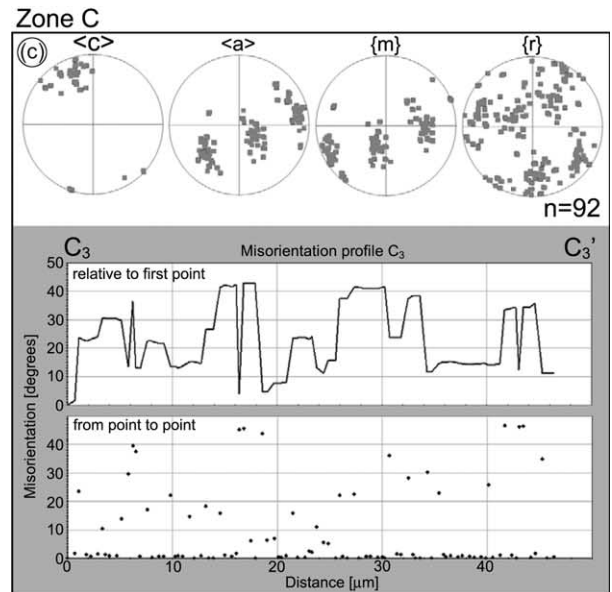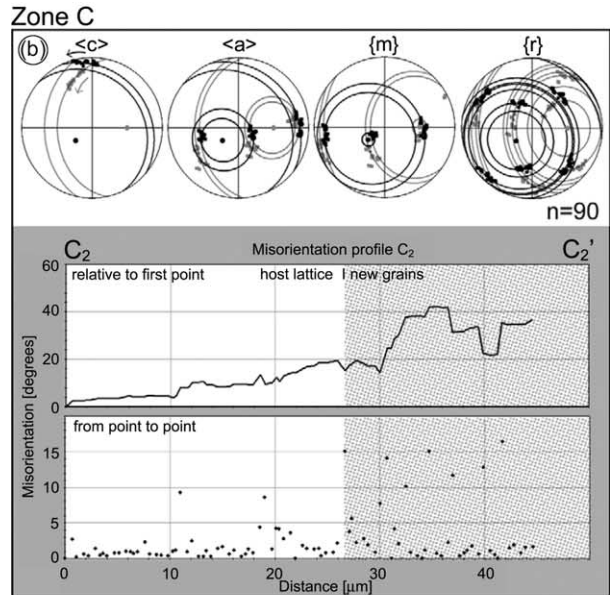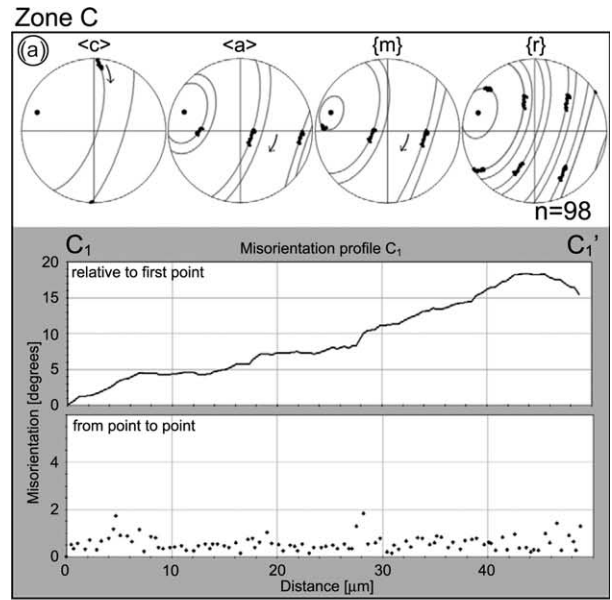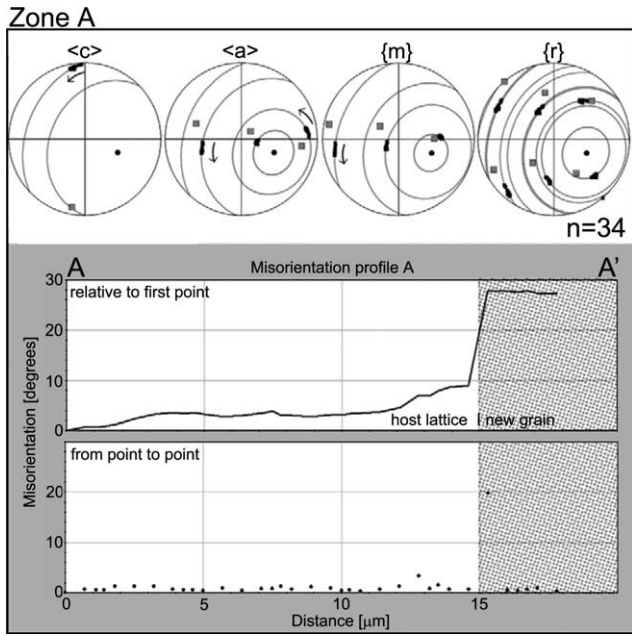
Fig. 8. Profile (A–A′). Its location in zone A (initial shear zone) is given in Fig. 6a. Top: change of orientation along the line is presented as dispersion patterns in pole figures (equal area, upper hemisphere). Host domains are black squares, new grains are grey squares. Grey small circles are calculated as best-fit rotation paths, black dots mark the best-fit rotation axes. Arrows indicate the sense of rotation from A to A′. Bottom: the continuous change in misorientation angles is displayed with respect to the first point and also from point to point. The domain with the new grain is stippled.

new grains within the shear zones and are all elongated roughly perpendicular to σ_1. They contain some subgrain boundaries, but no major orientation gradients. The host crystal rotates away from the starting orientation in a clockwise and an anticlockwise sense around a horizontal axis (Fig. 7d). The new grains scatter largely (up to 90° difference in c-axes) away from
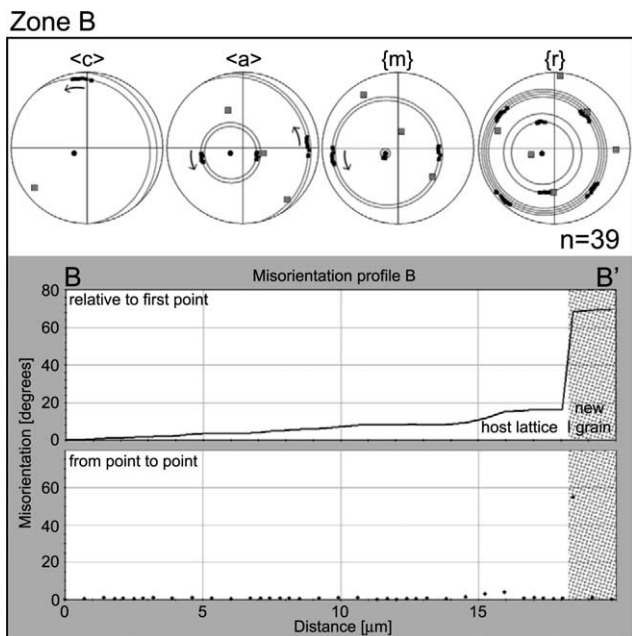

Fig. 9. Profile (B–B′). Its location in zone B (dextral mature shear zones) is given in Fig. 6b; same presentation as Fig. 8.
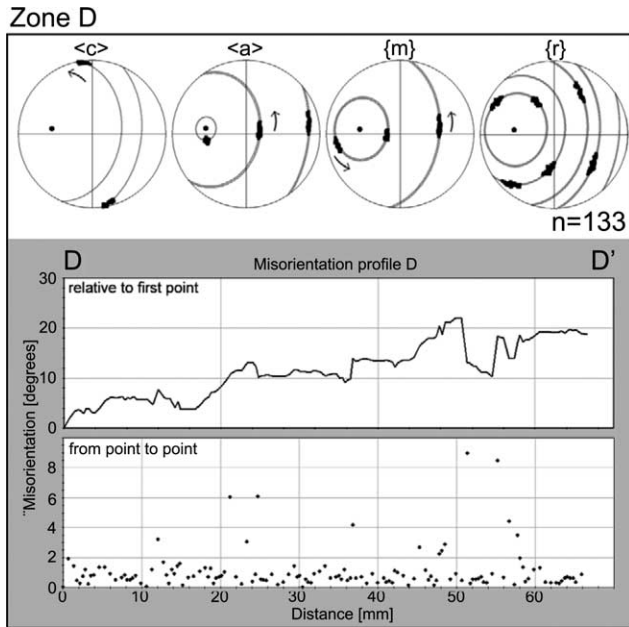
Fig. 11. Profile (D–D′). Its location in zone D (isolated patches of new grains) is given in Fig. 6d; same presentation as Fig. 8.

the host orientation and away from each other. The misorientation profile (Fig. 11), which crosses several subgrain boundaries with point to point misorientations up to 9°, shows an anticlockwise rotation of the host lattice around an axis close to ⟨a⟩ perpendicular to σ₁. Subgrain boundaries have the same rotation path as the host lattice.

3.3.6. Misorientation axes

Fig. 12a displays the distribution of the misorientation axes for different intervals of misorientation angle with respect to the crystal reference frame, covering the complete data set containing the host crystal and the new grains. Especially at low misorientation angles (<10°), but even up to 40°, ⟨a⟩ and the pole to {m} are equally favoured as misorientation axes. Misorientation angles up to 15° have a slight preference for ⟨a⟩ as a misorientation axis. Above 40° there is a rather homogeneous distribution of misorientation axes. Fig. 12b shows the distribution of misorientation axes with respect to the sample reference frame for the same intervals as in Fig. 12a. The plots show that especially for small misorientation angles (<15°), the misorientation axes cluster around an orientation that is perpendicular to σ₁ and about 60° away from the centre on the left side of the plot. Between 15 and 60°, the misorientation axes seem to be homogeneously distributed within the plane perpendicular to σ₁. Above 60°, there are too little misorientation axes to show a clear trend.

Fig. 10. Profiles (C₁–C₁′, C₂–C₂′ and C₃–C₃′). The locations in zone C (sinistral mature and transitional shear zones) are given in Fig. 6c; same presentation as Fig. 8.

4. Discussion

In this paper we aim at understanding how intracrystalline shear zones nucleate and further evolve in quartz during deformation in the presence of water. Strong CPOs and a dynamically recrystallised microstructure are often taken as an indication for a crystal-plastic origin of ductile shear zones (e.g. Urai et al., 1986; Passchier and Trouw, 1998; Fitz Gerald et al., in press). However, detailed EBSD analyses of naturally deformed rocks have shown that the misorientation relationship observed between parent and recrystallised grains cannot always be explained by the mechanisms of subgrain rotation and grain boundary migration recrystallisation alone (Leiss and Barber, 1999; Bestmann and Prior, 2003; Prior et al., 2004; Wheeler et al., 2004). Other processes may exert an important control on the misorientation between host and recrystallised grains. In the following we evaluate our EBSD and TEM data with respect to existing models and discuss conflicting observations.

4.1. Models for shear zone development

In a classical model for shear zone development including subgrain rotation recrystallisation a gradual build-up in misorientation along subgrain walls is expected (Poirier and Nicolas, 1975; Urai et al., 1986). Eventually the walls become a high enough angle to loose their internal structure and become grain boundaries. Most new grain boundaries would then be fairly low angle (but >10°) with respect to the host domains (Wheeler et al., 2004) and the new grains should display a rotation path that is similar to that of the host domains.

The rotation paths of the host domains and of the new grains within the shear zones studied in this paper are dissimilar. Grain misorientations are hardly related to grain or grain boundary crystallography, and the misorientation angles between host domains and new grains are generally large (up to 90°). Three alternative models were put forward to explain these large angle grain boundaries between new grains and host domains within shear zones. (1) Recrystallised grains, once formed by subgrain rotation, deform partly by diffusion accommodated grain boundary sliding (Bestmann and Prior, 2003). (2) New grains precipitate by growth from solution in intracrystalline microcracks (den Brok and Spiers, 1991; Hippertt and Egydio-Silva, 1996). (3) New grains are slightly rotated and translated fracture fragments that were broken off from the host grain (den Brok, 1992; Nyman et al., 1992; den Brok et al., 1998; van Daalen et al., 1999).

The first model is based on detailed EBSD data from naturally formed shear zones within a greenschist facies calcite marble (Bestmann and Prior, 2003). The model describes the development of new grains by subgrain rotation and subsequent deformation by grain boundary sliding. It therefore requires that subgrains have similar sizes as the new grains in the shear zones and that new grains progressively lose their misorientation relationship with nearby (sub)grains towards the centre of the shear zones. The misorientation axis of the grains at the shear zone boundaries should still be similar to that of the

subgrains and the host domains. The new grains in our studied sample are generally smaller than the subgrains and they have different misorientation axes than the subgrains and the host domains. Their CPO is much different to the orientation of the host domains. Therefore we cannot support an origin of the new grains from previous subgrains in the host.

The second model is based on optical observations in experimentally deformed quartzites (den Brok and Spiers, 1991) and in a naturally deformed greenschist facies quartz mylonite (Hippertt and Egydio-Silva, 1996). In this model, strain-free new grains nucleate and grow by precipitation from a solution in open microcracks. The new grains nucleate and grow with crystallographic orientations that are not necessarily dependent on the crystallographic orientation of the host grain. The crystallographic data of our studied sample gave clear evidence for progressive large angle rotation of the new grains with the sense of shear away from the host orientation in the shear direction, i.e. for a memory transferred from host grains to new grains.

The third model is based on optical analysis of experimentally deformed quartz (den Brok, 1992), naturally deformed amphibole (Nyman et al., 1992), 'in-situ' experimentally deformed salt (den Brok et al., 1998), as well as the combined analysis of computer-integrated polarisation (CIP) microscopy and EBSD-data on naturally formed shear zones within subgreenschist facies quartz fibres (van Daalen et al., 1999). In this model, microcracks form by slow water-assisted stress-corrosion. The fracture fragments subsequently rotate. van Daalen et al. (1999) showed that fracturing occurred preferentially along the rhomb planes in the deformed quartz fibres. Further movement along these cracks caused the material in between to break apart into fragments that rotate in a direction that is conformable with the applied shear, much like the so called 'fracture hypothesis' of CPO-development proposed by Sander (1911). According to this model, new grains are rotated and subsequently healed fracture fragments; small angle boundaries that are parallel to the rhomb planes are healed microcracks. Several observations in our experimentally deformed sample support the interpretation of microcracking leading to strain localisation and subsequent shear zone formation. These observations are: the presence of fluid inclusions between the new grains within the shear zones, the abundance of water-filled voids at the grain boundaries and at the subgrain walls and the rhombohedral orientation of subgrain boundaries and of entire shear zones. A preferred alignment of the cracks with the rhomb planes is inferred from the repeated coincidence of the traces of small angle boundaries with that of rhomb planes within the orientation map (Fig. 6). These planes are also in an orientation with the highest shear stress ($\sim 45°$ to σ_1). Intragranular shear zones along rhomb planes were also observed by van Daalen et al. (1999) in greenschist facies naturally deformed quartz. The relatively high porosity within the shear zones, the angular shape of the new grains and large jumps in crystallographic orientation between the new grains within the shear zones and the host domains suggest that the new grains are rotated
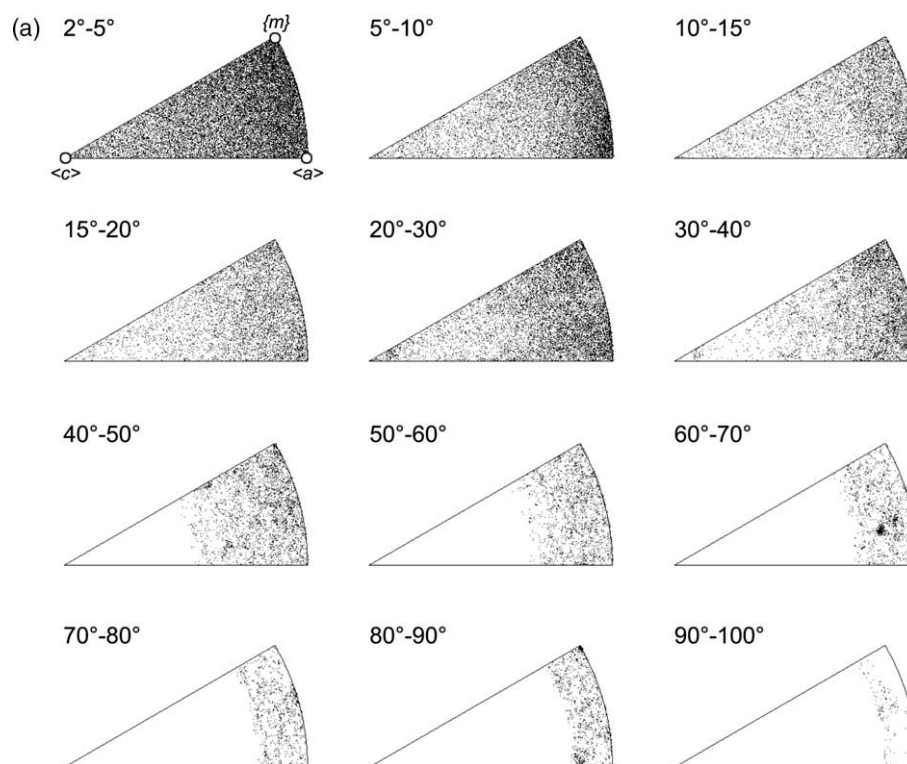

Fig. 12. Distribution of misorientation axes and angles for the whole analysed area (Fig. 5). Misorientation axes are displayed for fixed intervals of misorientation angle (a) with respect to the crystal reference frame (equal area, upper hemisphere projection, important crystallographic directions and planes are indicated by open circles) and (b) with respect to the sample reference frame (equal area, upper hemisphere projection).
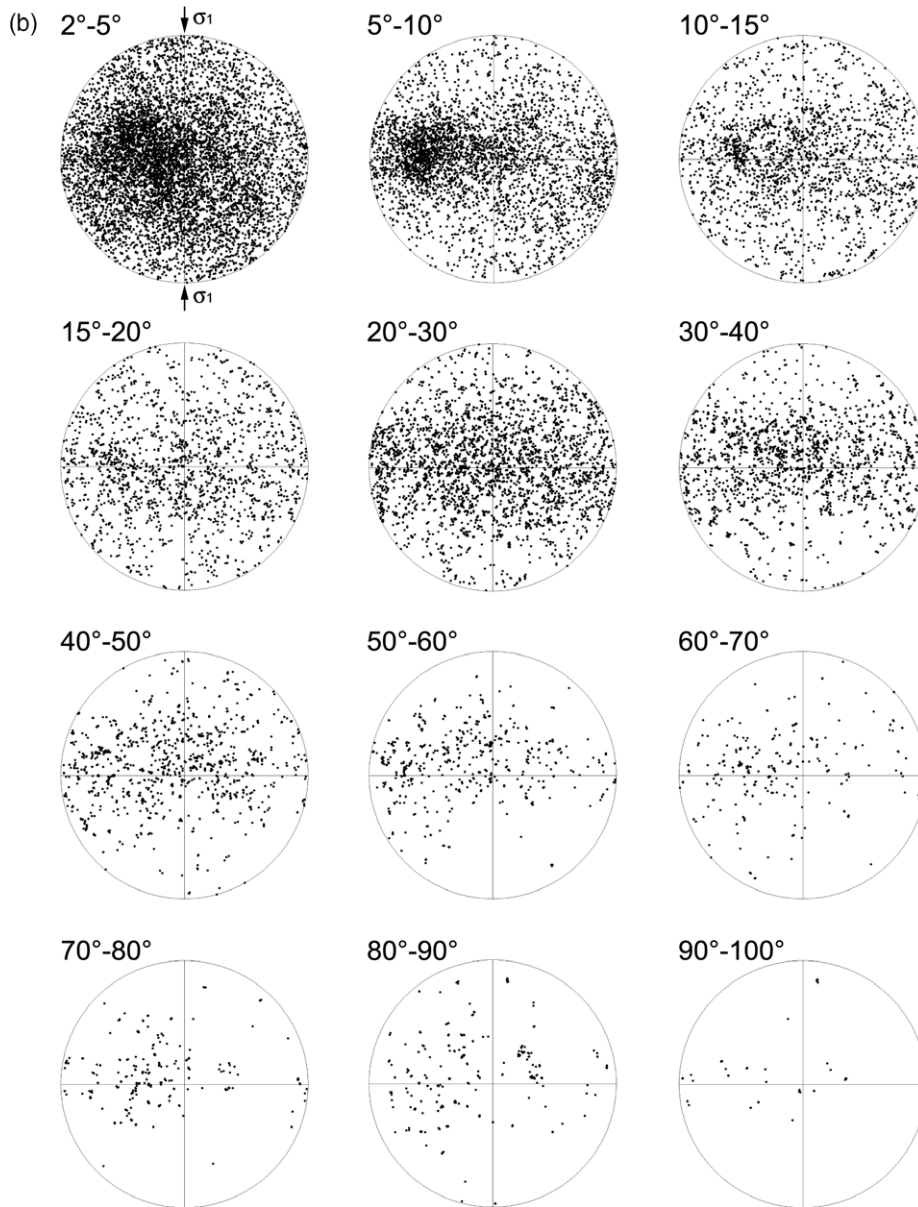
Fig. 12 (*continued*)

fracture fragments. The tangled dislocations at the grain boundaries may have formed in response to crack propagation.

4.2. Shear zone development in the studied sample

Our view on shear zone formation is therefore strongly based on the third model (Fig. 13). Because of the combined analysis of TEM images and high resolution EBSD data we are able to constrain the mechanisms of shear zone development in greater detail. During the initial phase of linear work hardening (Fig. 1), the stress increases to a relatively high value, because the crystal orientation prevents the conventional prism, basal and rhomb ⟨a⟩ slip systems from being easily activated in this sample. At the highest differential stress, planar microcracks start to develop parallel to the rhomb planes (Fig. 13a). Some

of the cracks heal after little rotational displacement (Fig. 4c) and are now observed as rhombohedral 'subgrain boundaries'. During the subsequent phase of weakening (Fig. 1), further microcracking along the rhomb planes (Figs. 6a and 13b) leads to shear zone development. During sliding, fracture fragments may slightly rotate around an axis perpendicular to σ_1 (Fig. 12b), heal and become 'subgrains', as was observed, for example, in in-situ experiments on brittle rock analogue materials (den Brok et al., 1998). Our observations (Figs. 8, 9 and 12b) suggest that these rotations are more related to the geometry and orientation of the shear zone than to grain or boundary crystallography. During sliding of the fracture fragments, the average misorientation between the subgrains and the host domains increases and misorientation axes are randomised. The fracture fragments become separate grains as
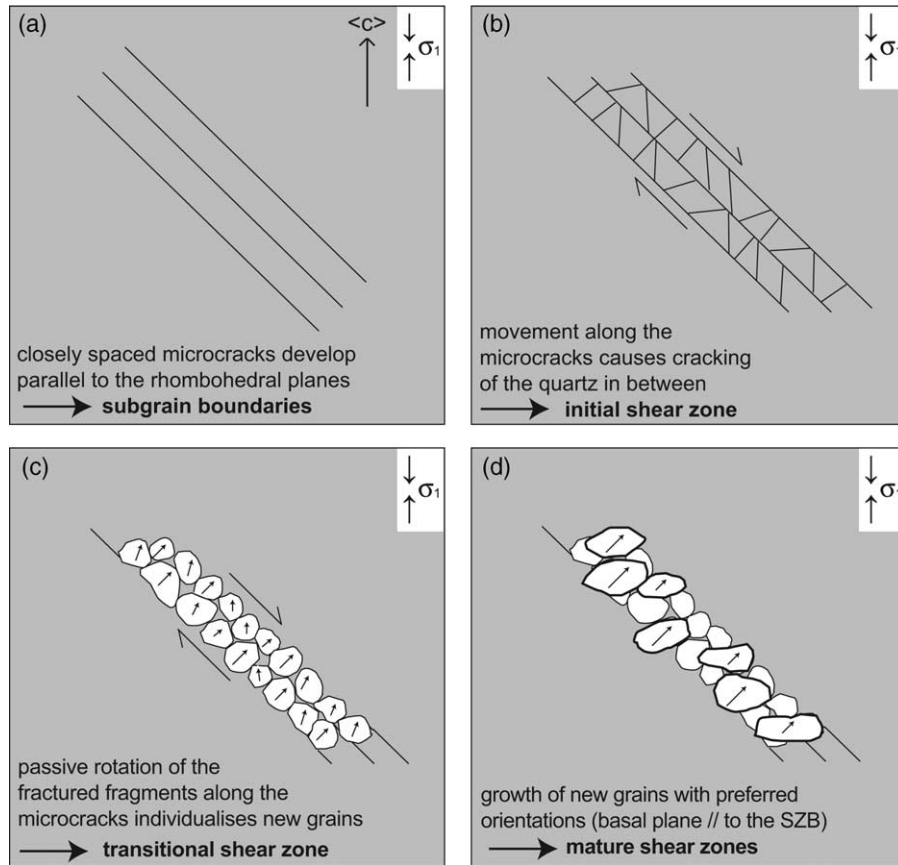
Fig. 13. Schematic model for the evolution of an intracrystalline shear zone in quartz. (a) Microcracks develop parallel to the rhomb planes. In the EBSD orientation maps such microcracks could be identified as aligned small angle boundaries in cases where rotational offsets were observed. (b) An initial shear zone develops during further microcracking. (c) Fracture fragments become new grains while rotating further in the direction of the shear zone. The rotation may be facilitated by the high water pressure and the relatively high porosity in the shear zone. (d) A strong CPO develops within mature shear zones, because new grains with $\langle c \rangle$ oriented perpendicular to the shear zone boundary start to grow at the cost of other new grains.

they further rotate in a direction conforming to the sense of shear (Fig. 13c). The rotation of the new grains is probably facilitated by the high water pressure and the relatively high water-filled porosity within the shear zones (Fig. 4a and b; see also Schmocker et al., 2003). The frozen microstructure of the sample is still transitional and reflects various stages of shear zone development. Therefore, the different microstructures (e.g. shown in Fig. 6a–d) could impossibly be related to different stages in the deformation curve (Fig. 1). The final phase of work hardening in the deformation curve is most probably an artefact, because the stress was not corrected for friction increase during the experiment and the strain was calculated using only the initial diameter of the sample.

4.3. Fabric development in the shear zones

The extension of new grains (with $\langle c \rangle$ perpendicular to the shear zone boundary) into the surrounding host (Figs. 3b and c and 6b) suggests relatively fast selective growth and grain boundary migration perpendicular to σ_1, which is related to extension in this direction and to the relatively high dislocation density in the host domains (Fig. 4c). Grain boundary migration is strongly enhanced if water is present on the

grain boundaries (e.g. Drury and Urai, 1990; Mancktelow and Pennacchioni, 2004). It may have caused the development of a strong CPO with c-axes preferentially aligned perpendicular to, and basal planes aligned parallel to the shear zone boundary (Fig. 13d). Apparently this orientation is favoured for growth. It is very commonly observed in quartz shear zones (e.g. Burg and Laurent, 1978; Simpson, 1980; Schmid and Casey, 1986) and generally interpreted to develop by preferred growth of grains that are suitably oriented for basal slip. The elongate shape of the new grains in these mature shear zones might be the result of subsequent deformation by slip along the basal plane in axial compression.

4.4. Isolated pockets of new grains

The above model for shear zone development does not explain the development of the new grains in isolated pockets (Fig. 6d). The geometry of the isolated pockets and the crystallographic orientations of the new grains clearly indicate that they did not rotate gradually out of the host orientation. Large grain boundary misorientations (up to 90° difference in c-axes) occur. We postulate that these new grains nucleated with high angle misorientation relative to the host domains

(see also Wheeler et al., 2004). The boundaries of the new grains have then migrated relatively fast in a direction perpendicular to σ_1. Our data cannot explain how the nuclei originate. However, because of the notable effect of the water on the deformation behaviour of the deformed sample, we suggest that they develop by precipitation from solution in small voids and microcracks like in the experiments of den Brok and Spiers (1991) and in the natural deformed quartz samples of Hippertt and Egydio-Silva (1996).

5. Summary and conclusions

This study yields the following conclusions:

(1) Uniaxial deformation of a quartz single crystal parallel to the *c*-axis in the presence of water, at a temperature of 800 °C, a confining pressure of ~ 1.2 GPa and a strain rate of $\sim 10^{-6}\,\mathrm{s}^{-1}$, led to the development of intracrystalline shear zones that reflect different stages of shear zone development.

(2) EBSD and TEM analyses complemented each other in providing a detailed picture of the operating deformation mechanisms in intracrystalline shear zones. The (sub)grain boundaries that were identified on EBSD orientation maps and image quality maps were independently verified on TEM images as being healed microcracks.

(3) The crystal initially deformed by intracrystalline plasticity, which became increasingly heterogeneously distributed. At the highest differential stress, microcracks developed parallel to the rhomb planes, at approximately 45° to the σ_1-direction. These microcracks are traced by fluid inclusions and are visible as small angle (subgrain) boundaries in the EBSD orientation maps. They must have healed after only little rotational displacement. Further microcracking along the rhomb planes led to shear zone development.

(4) 'New' grains developed during movement along the initial shear zones by sliding and rigid body rotation of the fracture fragments. Rotation took place in a direction conforming to the shear sense of the shear zone.

(5) A strong CPO developed by dynamic recrystallisation because of relatively fast preferred growth of new grains that have $\langle c \rangle$ perpendicular and the basal plane parallel to the shear zone boundary. Thereby they developed an elongated shape perpendicular to σ_1.

(6) New grains in isolated pockets probably developed by precipitation and subsequent growth out of solution.

Acknowledgements

References

Adams, B.L., Wright, S.I., Kunze, K., 1993. Orientation imaging—the emergence of a new microscopy. Metallurgical Transactions A—Physical Metallurgy and Materials Science 24 (4), 819–831.

Bagdassarov, N.S., Delépine, N., 2004. Alpha–beta inversion in quartz from low frequency electrical impedance spectroscopy. Journal of Physics and Chemistry of Solids 65 (8–9), 1517–1526.

Bestmann, M., Prior, D.J., 2003. Intragranular dynamic recrystallization in naturally deformed calcite marble: diffusion accommodated grain boundary sliding as a result of subgrain rotation recrystallization. Journal of Structural Geology 25 (10), 1597–1613.

Burg, J.P., Laurent, P., 1978. Strain analysis of a shear zone in a granodiorite. Tectonophysics 47 (1–2), 15–42.

den Brok, S.W.J., 1992. An experimental investigation into the effect of water on the flow of quartzite. Geologica Ultraiectina 95, 178.

den Brok, S.W.J., Spiers, C.J., 1991. Experimental evidence for water weakening by microcracking plus solution-precipitation creep. Journal of the Geological Society, London 148, 541–548.

den Brok, S.W.J., Zahid, M., Passchier, C., 1998. Cataclastic solution creep of very soluble brittle salt as a rock analogue. Earth and Planetary Science Letters 163, 83–95.

Drury, M.R., Urai, J.L., 1990. Deformation-related recrystallization processes. Tectonophysics 172 (3–4), 235–253.

Fitz Gerald, J.D., Mancktelow, N.S., Pennacchioni, G., Kunze, K., in press. Ultra-fine grained quartz mylonites from high-grade shear zones: evidence for a strong dry mid-to-lower crust. Geology.

Hippertt, J., Egydio-Silva, M., 1996. New polygonal grains formed by dissolution-redeposition in quartz mylonite. Journal of Structural Geology 18 (11), 1345–1352.

Kunze, K., Schaeben, H., 2004. The Binghan distribution of quaternions and its spherical Radan transform in texture analysis Mathematical Geology. 36 (8): 917–943.

Leiss, B., Barber, D.J., 1999. Mechanisms of dynamic recrystallization in naturally deformed dolomite inferred from EBSP analyses. Tectonophysics 303 (1–4), 51–69.

Mancktelow, N.S., Pennacchioni, G., 2004. The influence of grain boundary fluids on the microstructure of quartz–feldspar mylonites. Journal of Structural Geology 26 (1), 47–69.

Nyman, M.W., Law, R.D., Smelik, E.A., 1992. Cataclastic deformation mechanism for the development of core–mantle structures in amphibole. Geology 20 (5), 455–458.

Passchier, C.W., Trouw, R.A.J., 1998. Microtectonics. Springer, Berlin. 289pp.

Paterson, M.S., 1982. The determination of hydroxyl by infrared-absorption in quartz, silicate-glasses and similar materials. Bulletin De Mineralogie 105 (1), 20–29.

Poirier, J.P., Nicolas, A., 1975. Deformation-induced recrystallization due to progressive misorientation of subgrains, with special reference to mantle peridotites. Journal of Geology 83 (6), 707–720.

Prentice, M.J., 1986. Orientation statistics without parametric assumptions. Journal of the Royal Statistical Society. B 48 (2): 214–222.

Prior, D.J., Boyle, A.P., Brenker, F., Cheadle, M.C., Day, A., Lopez, G., Peruzzo, L., Potts, G.J., Reddy, S., Spiess, R., Timms, N.E., Trimby, P., Wheeler, J., Zetterstrom, L., 1999. The application of electron backscatter diffraction and orientation contrast imaging in the SEM to textural problems in rocks. American Mineralogist 84 (11–12), 1741–1759.

Prior, D.J., Bestmann, M., Halfpenny, A., Mariani, E., Piazolo, S., Tullis, J., Wheeler, J., 2004. Recrystallization and grain growth in rocks and minerals. In: Recrystallization and Grain Growth, Pts 1 and 2. Materials Science Forum 467–470, 545–550.

Ralser, S., 1990. Shear zones developed in an experimentally deformed quartz mylonite. Journal of Structural Geology 12 (8), 1033–1045.

Ramsay, J.G., 1980. Shear zone geometry—a review. Journal of Structural Geology 2 (1–2), 83–99.

Sander, B., 1911. Ueber zusammenhänge zwischen Teilbewegung und Gefüge in Gesteinen. Tschermaks Mineralogische Petrografische Mitteilungen 30, 281–314.

Schmid, S.M., Casey, M., 1986. Complete fabric analysis of some commonly observed quartz c-axis patterns. In: Hobbs, B.E., Heard, H.C. (Eds.), Mineral and Rock Deformation: Laboratory Studies. The Paterson Volume Geophysical Monograph 36, pp. 263–286.

Schmocker, M., Bystricky, M., Kunze, K., Burlini, L., Stunitz, H., Burg, J.P., 2003. Granular flow and Riedel band formation in water-rich quartz aggregates experimentally deformed in torsion. Journal of Geophysical Research-Solid Earth 108 (B5), 2242. doi:10.1029/2002JB001958.

Segall, P., Simpson, C., 1986. Nucleation of ductile shear zones on dilatant fractures. Geology 14 (1), 56–59.

Simpson, C., 1980. Oblique girdle orientation patterns of quartz c-axes from a shear zone in the basement core of the Maggia–Nappo–Ticino, Switzerland. Journal of Structural Geology 2 (1–2), 243–247.

Urai, J.L., Means, W.D., Lister, G.S., 1986. Dynamic recrystallization of minerals. In: Hobbs, B.E., Heard, H.C. (Eds.), Mineral and Rock Deformation: Laboratory Studies. The Paterson Volume Geophysical Monograph 36, pp. 161–199.

van Daalen, M., Heilbronner, R., Kunze, K., 1999. Orientation analysis of localized shear deformation in quartz fibres at the brittle–ductile transition. Tectonophysics 303, 83–107.

Vernooij, M.G.C., 2005. Dynamic recrystallisation and microfabric development in single crystals of quartz during experimental deformation. PhD thesis ETH Zürich, http://e-collection.ethbib.ethz.ch.

Vernooij, M.G.C., Langenhorst, F., 2005. Experimental reproduction of tectonic deformation lamellae and comparison to shock-induced planar deformation features. Meteoritics & Planetary Science 40 (9–10), 1353–1361.

Wheeler, J., Prior, D.J., Jiang, Z., Spiess, R., Trimby, P.W., 2001. The petrological significance of misorientations between grains. Contributions to Mineralogy and Petrology 141 (1), 109–124.

Wheeler, J., Jiang, Z.T., Prior, D., Tullis, J., 2004. Dynamic recrystallisation of quartz. In: Recrystallization and Grain Growth, Pts 1 and 2. Materials Science Forum 467–470, 1243–1248.

White, S., 1977. Geological significance of recovery and recrystallization processes in quartz. Tectonophysics 39 (1–3), 143–170.